

---

# Causal integration of chemical structures improves representations of microscopy images for morphological profiling

---

Yemin Yu<sup>1\*</sup> Neil Tenenholtz<sup>2</sup> Lester Mackey<sup>2</sup> Ying Wei<sup>3</sup> David Alvarez-Melis<sup>2</sup>  
Ava P. Amini<sup>2</sup> Alex X. Lu<sup>2</sup>

<sup>1</sup> City University of Hong Kong <sup>2</sup> Microsoft Research <sup>3</sup> Zhejiang University

\* Work primarily done during an internship at Microsoft Research

yeminyu2-c@cityu.edu.hk, ying.wei@zju.edu.cn

{neil.tenenholtz,lmackey,alvarez.melis,ava.amini,lualex}@microsoft.com

## Abstract

Recent advances in self-supervised deep learning have improved our ability to quantify cellular morphological changes in high-throughput microscopy screens, a process known as morphological profiling. However, most current methods only learn from images, despite many screens being inherently multimodal, as they involve both a chemical or genetic perturbation as well as an image-based readout. We hypothesized that incorporating chemical compound structure during self-supervised pre-training could improve learned representations of images in high-throughput microscopy screens. We introduce a representation learning framework, MICON (Molecular-Image Contrastive Learning), that models chemical compounds as treatments that induce counterfactual transformations of cell phenotypes. MICON significantly outperforms classical hand-crafted features such as CellProfiler and existing deep-learning-based representation learning methods in challenging evaluation settings where models must identify reproducible effects of drugs across independent replicates and data-generating centers. We demonstrate that incorporating chemical compound information into the learning process provides consistent improvements in our evaluation setting and that modeling compounds specifically as treatments in a causal framework outperforms approaches that directly align images and compounds in a single representation space. Our findings point to a new direction for representation learning in morphological profiling, suggesting that methods should explicitly account for the multimodal nature of microscopy screening data.

## 1 Introduction

High-throughput microscopy experiments have become instrumental to drug discovery, guided by the principle that changes in cellular morphology can give insight into drug efficacy and mechanism of action [23, 39]. By coupling scalable fluorescent staining methods like Cell Painting [3] with large libraries of small molecules and high-throughput instrumentation, researchers can screen millions of compounds in cell lines, with the aim of identifying drugs that elicit desired effects based on morphological cues. Recent advances in computer vision promise to automate the quantification of increasingly subtle morphological changes [4, 30]. The goal of these computational methods is to convert an image into a vector of features, or a representation, that captures cell phenotype, a process called morphological profiling. Representations facilitate the quantitative comparison of phenotypes in microscopy images, which are typically not directly comparable in raw pixel space.

For example, to nominate candidate drugs, a researcher might seek to use morphological profiling to identify compounds that yield similar representations — and therefore similar phenotypes — to known effective drugs.

Hand-crafted features, made accessible by the CellProfiler [7] software, have traditionally been used to construct these representations. However, these coarse features often fail to pick up on subtle morphological changes and are confounded by microscopy batch effects that cause irreproducible technical variation. The need for high-quality, robust representations has led researchers to investigate deep-learning based representation learning methods [36]. Since labels for morphological profiling are scarce and frequently unreliable, many representation learning methods train using self-supervised learning, which aims to learn high-quality representations without labeled training data [32]. For morphological profiling, previous studies have explored various self-supervised frameworks [18], including contrastive learning [9, 29, 22], masked autoencoding [16, 20], and self-distillation [6, 12].

While representation learning approaches have shown improvements in sensitivity and robustness relative to hand-crafted features, most methods learn from images exclusively. However, microscopy-based drug screens are inherently multimodal: perturbations, which may be chemical, genetic, or environmental, are used to induce phenotypic changes in cells. Few works have investigated how integrating multimodal information about perturbations, such as the identities of chemical compounds, can improve representation learning. Some weakly supervised methods predict perturbation identity as a target during training [5], but these methods only use the identity of the chemical compound and not any information about its structure. CLOOME [34] and MolPhenix [13] integrate chemical structure information through a CLIP (Contrastive Language Image Pre-training) [31] objective to align images and chemical compounds in a unified representation space that enables querying of data from one modality given the other. However, morphological phenotypes and chemical compounds are not directly comparable; for example, depending on cell type, cells may produce different phenotypic responses to the same compound. This may create tensions where a single representation of a chemical compound must be aligned to multiple representations across a dynamic range of phenotypic responses.

Rather than assuming cell phenotypes in images and chemical compounds to be directly comparable, we instead model chemical compounds as *treatments* that induce counterfactual transformations of microscopy images to develop MICON (Molecular-Image Contrastive Learning), a self-supervised, causal representation learning framework for morphological profiling (Figure 1). Given an image of unperturbed cells and a chemical compound, MICON learns how to generate a representation corresponding to a phenotypic transformation of the cells in the image, as if they had been treated with the compound. Using the MICON framework, we controllably test the hypothesis that integrating chemical compound information can improve image representation learning in morphological profiling. First, we show that MICON achieves effective representation learning, substantially improving over both CellProfiler features and previously proposed deep learning methods. Second, through ablation of MICON’s multimodal component, we demonstrate that integrating chemical compound information provides a consistent improvement in performance relative to learning from images alone. Finally, supporting our hypothesis that *how* multimodal information is integrated is crucial, we show that modeling chemical compounds as treatments in a counterfactual framework significantly outperforms direct alignment of images and compounds with a CLIP objective. Our results advocate for approaching morphological profiling as a multimodal learning problem and provide insight into how to best integrate images and perturbations.

## 2 Methods

### 2.1 MICON: Molecular-Image Contrastive Learning

MICON is a novel representation learning method for morphological profiling experiments that integrates chemical compounds and images into a multimodal pre-training task (Figure 1). MICON models chemical compounds as treatments that induce a counterfactual transformation in images. Given an image of untreated control cells and a chemical compound, our method transforms the cells in the image as if they had been treated with the chemical compound. In other words, we train MICON to simulate the phenotypic effects of chemical compounds, given a chemical compound and an image of untreated cells as input. We perform this transformation directly in the image representation space, using contrastive losses to align counterfactual and real representations (Figure 1A). We next

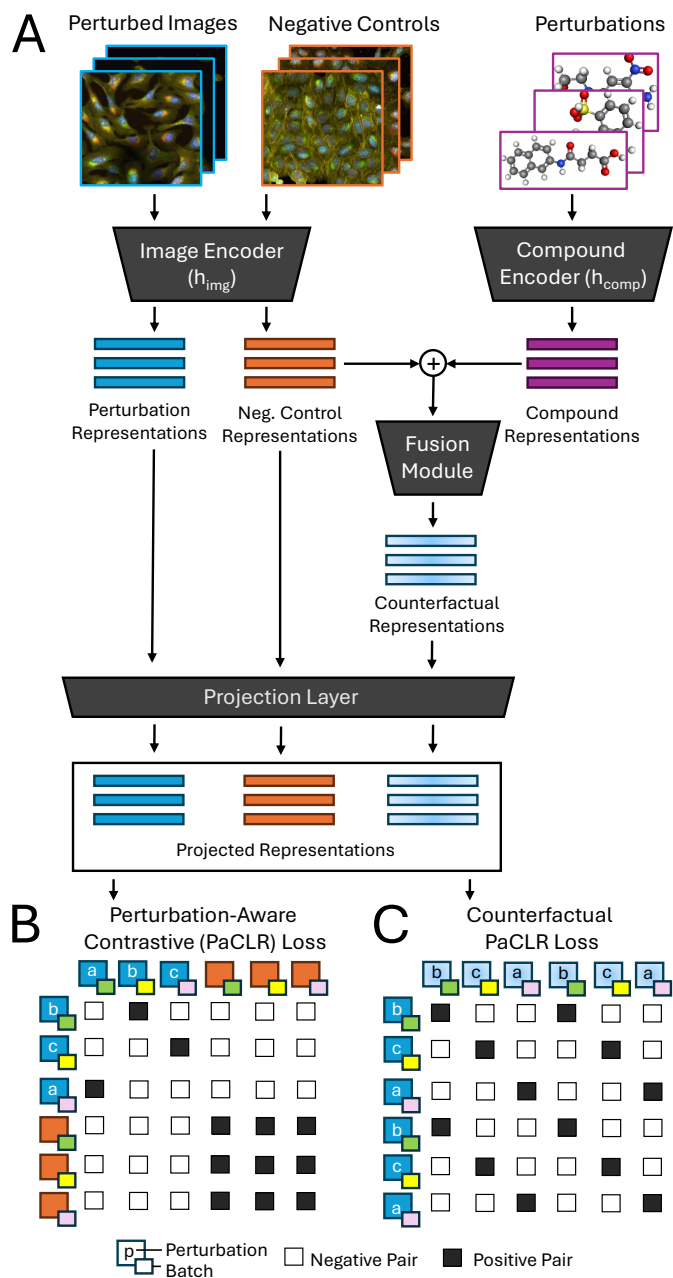


Figure 1: **Summary of the MICON framework.** (A) An overview of our model. Compound perturbed (blue) images and negative control (orange) images are transformed into representations by an image encoder, while chemical compounds (purple) are transformed into representations by a compound encoder. A fusion module accepts pairs of negative control representations and compound representations and outputs counterfactual representations (light blue). All representations are passed through a projection layer to form the final projected representations. (B) Summary of the perturbation-aware contrastive (PAC) loss. Perturbed images (blue) and negative controls (orange) from the same batches as the perturbed images (batches denoted by small colored boxes) are sampled, with at least two images for each perturbation. Images treated with the same perturbation (a, b, or c) serve as positive pairs (black squares) for the PaCLR loss. (C) Summary of the counterfactual PaCLR loss. Perturbation representations (blue) and generated counterfactual representations (light blue) using the same compound (a, b, or c) serve as positive pairs (black squares) for the counterfactual PaCLR loss.

describe the two components of our representation learning approach: a perturbation-aware contrastive learning objective that learns faithful representations of phenotypes in real microscopy images and a counterfactual perturbation-aware contrastive objective that aligns counterfactual representations and perturbation representations.

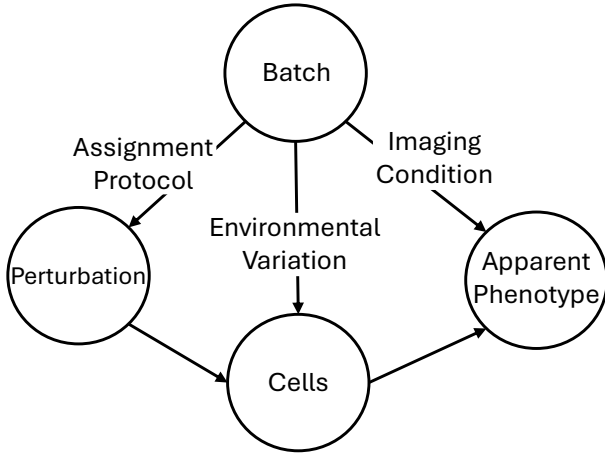


Figure 2: **Causal diagram of apparent phenotype in image-based perturbation profiling.** In addition to a perturbation treatment’s effect on cells and, in turn, apparent phenotypes, microscopy batch effects can impart multiple layers of impact: at the levels of perturbation treatment, cell phenotype, and apparent imaging phenotype.

### 2.1.1 Perturbation-Aware Contrastive Learning of Representations

As our method relies on alignment of counterfactual and perturbation representations, we must first ensure that representations of real phenotypes are robust and capture the phenotypic effects of perturbations. However, learning such a representation is challenging because of microscopy batch effects (or technical variation) that can impact the apparent phenotype of cells in images [2]. As shown by our causal diagram (Figure 2), batch effects can influence microscopy images in multiple ways, introducing variation into both true phenotypes, due to factors such as variation in the environment of the cells, and the appearance of those phenotypes in images, due to factors such as variation in imaging protocol or instrument. Thus, the phenotypic effects of perturbations are confounded by microscopy batch effects.

Batch effects are known to be a major confounder even in replicates at the same data-generating institution [4]. Our work leverages a dataset (cpg0016, see Section 2.2.1) where images are supplied by multiple sources, which introduces further differences between experiments (e.g., images may be collected under different microscopes) and thus even more severe microscopy batch effects [2]. If representations of real phenotypes are not robust to microscopy batch effects, counterfactual representations may instead be aligned according to differences in images introduced by technical variation, not the perturbation, reducing the efficacy of the counterfactual objective. To learn representations robust to batch effects, we design a Perturbation-Aware Contrastive Learning of Representations (PaCLR) objective, which leverages metadata about perturbation and microscopy batches to sample positive and negative pairs for contrastive learning.

We first consider a more standard self-supervised contrastive learning objective, i.e. SimCLR [9]. SimCLR trains using self-augmented pairs of images. In this setting, an image  $\mathbf{x}$  is encoded by an image encoder  $\mathbf{h}_{\text{img}}$ , then passed through a projection head  $g$  to obtain a projected representation  $\mathbf{t} = g(\mathbf{h}_{\text{img}}(\mathbf{x}))$ . Given  $N$  images with projected representations  $\mathbf{t}_1, \dots, \mathbf{t}_N$ , a contrastive loss can be used to pull together the representation of an image and its augmentations (positive pairs), while repelling representations of dissimilar images (negative pairs). For a given image index  $i$ , we let  $j$  index a differently augmented version of the same image and  $k$  iterate over all images other than  $i$  in the set (where  $k \neq j$  are assumed to be dissimilar to  $i$ ). The contrastive loss is then given by

$$\mathcal{L}_{i,j} = -\log \frac{\exp(\tau^{-1} \text{sim}(\mathbf{t}_i, \mathbf{t}_j))}{\sum_{k=1}^N \mathbb{1}_{[i \neq k]} \exp(\tau^{-1} \text{sim}(\mathbf{t}_i, \mathbf{t}_k))},$$

where  $\tau$  is the temperature scale hyperparameter for the softmax function and `sim` is a similarity measure (in our work, the cosine distance).

This naive contrastive strategy poses two problems in the context of morphological profiling. The first is class collision. In the above setting, all other images in a training batch are considered negative samples and equally repelled from the augmented pair of images. In high-throughput imaging however, some images in the same training batch may share the same perturbation and thus carry related morphological changes that we wish to capture. Second, augmented pairs of images are still likely to share microscopy batch effects, which makes a standard contrastive strategy prone to learning confounding technical variation, instead of focusing on the effect of the perturbation alone.

By leveraging metadata about the perturbation and microscopy batch to sample pairs for contrastive learning, the PaCLR loss addresses both of these issues (Figure 1B). First, we use metadata about perturbations to define positive pairs as instances perturbed by the same compound. Instead of using different augmented views of a single instance, we use images of the same perturbation as positive pairs. The underlying assumption is that, if the network learns to align two images of the same perturbation, the shared signal that is learned should be the biological signal, rather than confounding microscopy batch effects (since these images are drawn uniformly from the dataset, positive pairs can come from different microscopy batches, although this is not strictly enforced). Second, we use metadata about microscopy batch to sample negative control images (which are not treated with any compound, but rather a control treatment of only the solvent in which compounds are dissolved in). This means there are samples that share microscopy batch effects, but not perturbation, serving as negative examples, further encouraging the model to be robust to microscopy batch effects. We sample negative control images such that they come from the same microscopy plate as perturbed images or from the same microscopy batch as a fall-back for the rare case that there are no viable control images on the same plate (see Section 2.2.1 for a description of the structure of microscopy experiments). In addition to image instances perturbed by different compounds, these negative control images act as negative pairs in training, which further discourages the MICON model from learning about microscopy batch effects, as negative pairs are enforced to come from the same microscopy batches as perturbed images.

The above is implemented through sampling of batches during training. Given an image  $\mathbf{x}$ , let  $\mathbf{p}$  be its perturbation, and  $\mathbf{b}$  be its microscopy batch identifier. We first sample  $T$  perturbed images from the entire dataset to form the subset  $\mathcal{T}_1 = \{\mathbf{x}_1^{\mathcal{T}_1}, \dots, \mathbf{x}_T^{\mathcal{T}_1}\}$ . Next, for each image in  $\mathcal{T}_1$ , we sample a second distinct image from the dataset with the same perturbation to form the subset  $\mathcal{T}_2 = \{\mathbf{x}_1^{\mathcal{T}_2}, \dots, \mathbf{x}_T^{\mathcal{T}_2}\}$ , so  $\mathbf{p}_j^{\mathcal{T}_1} = \mathbf{p}_j^{\mathcal{T}_2}$  but  $\mathbf{x}_j^{\mathcal{T}_1} \neq \mathbf{x}_j^{\mathcal{T}_2}$ . Finally, we sample  $C$  negative control images from the dataset to form the subset  $\mathcal{C} = \{\mathbf{x}_1^{\mathcal{C}}, \dots, \mathbf{x}_C^{\mathcal{C}}\}$ , such that their microscopy batch identifiers match as many of the perturbed images ( $\mathcal{T}_1 \cup \mathcal{T}_2$ ) as possible given the size of the subset:  $\mathbf{b}_j^{\mathcal{C}} \in \{\mathbf{b}_1^{\mathcal{T}_1}, \dots, \mathbf{b}_T^{\mathcal{T}_1}\} \cup \{\mathbf{b}_1^{\mathcal{T}_2}, \dots, \mathbf{b}_T^{\mathcal{T}_2}\}$ , and  $|\{\mathbf{b}_1^{\mathcal{C}}, \dots, \mathbf{b}_C^{\mathcal{C}}\}| = \min(|\{\mathbf{b}_1^{\mathcal{T}_1}, \dots, \mathbf{b}_T^{\mathcal{T}_1}\} \cup \{\mathbf{b}_1^{\mathcal{T}_2}, \dots, \mathbf{b}_T^{\mathcal{T}_2}\}|, C)$ . Putting these together, the training batch is the union of these three subsets  $\mathcal{T}_1 \cup \mathcal{T}_2 \cup \mathcal{C}$ .

Finally, we extract a representation  $\mathbf{t}_i = g(\mathbf{h}_{\text{img}}(\mathbf{x}_i))$  from each image  $\mathbf{x}_i$  using our image encoder  $\mathbf{h}_{\text{img}}$ . With this notation in hand, we define the PaCLR loss,

$$\mathcal{L}_{\text{PAC}}^{\text{orig}} = -\frac{1}{N} \sum_{i=1}^N \frac{1}{\sum_{k=1}^N \mathbb{1}_{[\mathbf{p}_i = \mathbf{p}_k, i \neq k]}} \sum_{j=1}^N \mathbb{1}_{[\mathbf{p}_i = \mathbf{p}_j, i \neq j]} \log \frac{\exp(\tau^{-1} \text{sim}(\mathbf{t}_i, \mathbf{t}_j))}{\sum_{k=1}^N \mathbb{1}_{[i \neq k]} \exp(\tau^{-1} \text{sim}(\mathbf{t}_i, \mathbf{t}_k))}. \quad (1)$$

Note that for the purposes of our PaCLR loss, we treat negative control images identically to any perturbation image, so the two are only distinguished during sampling. The use of negative controls distinguishes our work from prior multimodal work for morphological profiling that used only perturbed images in learning [34]. We incorporate negative controls because, due to their lack of perturbation treatment, they primarily represent apparent phenotypic changes caused by batch effects and thus enable disentanglement of batch effects from perturbation effects.

### 2.1.2 Counterfactual Perturbation-Aware Contrastive Objective

To incorporate chemical compound information into MICON’s learning objective, we first encode chemical compounds into representations using a compound encoder  $\mathbf{h}_{\text{comp}}$  (Figure 1A). A fusion module  $F$  combines the resulting representations of chemical compounds with the representation of a control image. The fusion module is trained to output counterfactual representations that should reflect what images of cells would look like if the cells were to be treated with a given perturbation (Figure 1A). The counterfactual representations are aligned with true perturbation representations, which represent images of cells actually treated with a compound, using a variant of the perturbation-aware contrastive loss. Unlike the original PaCLR loss (Equation (1)), this PaCLR loss is calculated using only perturbation representations, i.e., excluding the negative controls (Figure 1C). However, the control images used to generate counterfactual representations in the fusion module are sampled such that they come from the same microscopy batches as the perturbation representations.

Formally, we use a fusion model  $F$  to combine the representation of a chemical compound  $\tilde{\mathbf{p}}$  and the representation of a negative control image  $\mathbf{x}^c$  into a counterfactual representation  $\tilde{\mathbf{t}} = F(g(\mathbf{h}_{\text{img}}(\mathbf{x}^c)), \mathbf{h}_{\text{comp}}(\tilde{\mathbf{p}}))$ . Then, given  $N/2$  perturbation representations and their perturbation treatments, denoted as the tuple  $(\mathbf{t}_i, \mathbf{p}_i)$ , and  $N/2$  counterfactual representations and their perturbation treatments, denoted as the tuple  $(\tilde{\mathbf{t}}_j, \tilde{\mathbf{p}}_j)$ , we define the following counterfactual PaCLR loss over the counterfactual representations and the perturbation representations:

$$\mathcal{L}_{\text{PaCLR}}^{\text{cf}} = -\frac{2}{N} \sum_{i=1}^{N/2} \frac{1}{\sum_{k=1}^{N/2} \mathbb{1}_{[\mathbf{p}_i = \tilde{\mathbf{p}}_k]}} \sum_{j=1}^{N/2} \mathbb{1}_{[\mathbf{p}_i = \tilde{\mathbf{p}}_j]} \log \frac{\exp(\tau^{-1} \text{sim}(\mathbf{t}_i, \tilde{\mathbf{t}}_j))}{\sum_{k=1}^{N/2} \exp(\tau^{-1} \text{sim}(\mathbf{t}_i, \tilde{\mathbf{t}}_k))}.$$

The final loss for MICON combines the original and counterfactual PaCLR objectives:

$$\mathcal{L} = \mathcal{L}_{\text{PaCLR}}^{\text{orig}} + \mathcal{L}_{\text{PaCLR}}^{\text{gen}}$$

## 2.2 Datasets, Stratification, and Preprocessing

### 2.2.1 Dataset

We leverage the JUMP Cell Painting Consortium’s (JUMP-CP) cpg0016 dataset, a large-scale dataset of approximately 8.1 million cell painting microscopy images of drug-treated U2-OS cells [8]. cpg0016 consists of data from 12 data-generating sources, enabling us to test robustness to microscopy batch effects more extensively than other cell painting datasets that consist of data from a single source.

Each source collects images of cells cultured on *plates*, which are sub-divided into 384 or 1536 *wells*, where each well is capable of containing an independent experiment treated with a different perturbation. A robot-controlled microscope takes images of the experiment in each well, typically multiple images of different parts of the well, where each distinct image of the same well is a *field of view (FOV)*. Plates are further organized into *batches*, which we term a *microscopy batch* to distinguish from a batch of data for model training, where plates in the same microscopy batch are imaged on the same day. While performing the same perturbation experiment across different wells, plates, microscopy batches, or sources can all generate microscopy batch effects, microscopy batch effects are generally considered more pronounced across different microscopy batches or sources, as opposed to different wells on the same plate, or different plates in the same microscopy batch [2].

The cpg0016 dataset contains several kinds of plates and wells, and we highlight those used in our study. First, the Compound plates form the majority of the dataset, and across all 12 sources, collectively represent multiple replicates of 116,750 compound perturbations. On each Compound plate, there are 32 wells dedicated to 4 replicates of 8 positive control compound treatments (abbreviated as POS-CTL in this work), which are 8 compounds selected to have the most distinct morphological changes from a pilot study. Second, the JUMP-Target-2-Compound plates (abbreviated as Target-2 in this work) are 301 compounds selected as likely to induce phenotypic effects in cells, and are performed in replicate by every source. Finally, every plate (including the Compound and Target-2 plates) include negative control wells treated with Dimethyl Sulfoxide (DMSO), the solvent used for all compound perturbations, which acts as a control when no compound is dissolved in DMSO. Further details on the dataset and data generation setup can be found in the original JUMP-CP paper [8].

For our experiments, we primarily use the POS-CTL wells and the Target-2 plates, with a small subset of compounds sampled from the Compound plates (see 2.2.2), not the full cpg0016 dataset.

### 2.2.2 Evaluation Strategy and Data Stratification

We evaluate representations using compound-replicate matching, a standard strategy for evaluating if representations robustly identify phenotypes in the presence of microscopy batch effects [4, 10]. The principle underlying compound-replicate matching is that cells treated with the same perturbations should have similar phenotypes, and therefore have similar representations, even if experiments originate from different microscopy batches or sources. Compound-replicate matching is typically implemented through nearest-neighbor retrieval [10, 24, 1, 17], which means for data stratification, in addition to defining *training* and *validation* datasets for representation learning, we also need to define compound-replicate matching *retrieval* and *query* datasets for evaluation. During evaluation, we retrieve the nearest neighbor in the retrieval dataset for each well from the query dataset, and measure whether these share the same perturbation treatment. There should be no overlap between the query dataset and each of the model training and validation datasets, to avoid overfitting to images seen during representation learning.

Our data stratification strategy is motivated by two guiding use cases for morphological profiling: first, the identification of reproducible biological changes in unseen data for sources and compounds seen during training, which we refer to as “in-distribution (ID) generalization”; and second, the identification of these changes in unseen data for sources and compounds **not** seen during training, which we refer to as “out-of-distribution (OOD) generalization”. The first use case captures scenarios such as those when a source trains a model on its own data and then seeks to evaluate it on newly-produced data. The second use case captures settings such as those when a distinct source seeks to use a pre-existing model, trained on data from other sources, to analyze their data, or when a source seeks to use a pre-existing model on new compounds not seen in training. To capture ID and OOD performance for *both* unseen sources and unseen compounds, we produce four distinct data splits on different subsets of data within the cpg0016 dataset (Figure 3, 4).

We use the POS-CTL dataset to evaluate model generalization to unseen sources (Figure 3A). We stratify the dataset by source in two ways to test ID and OOD performance (Figure 3B-C, with metadata about splits available in Supplementary Table A5). For the ID setting (Figure 3B), we use the 6 cpg0016 sources that have at least 10 POS-CTL plates. We train the MICON representation learning model on a subset of data from all 6 sources stratified by microscopy batch, and we hold out one batch from each source as validation data for model selection. This training dataset is recycled as the retrieval dataset, but we reserve unseen batches from all 6 sources as the query dataset (Figure 3B; Supplementary Table A5). We split microscopy batches into the retrieval dataset versus the query dataset at a 85-15 ratio. For the OOD setting (Figure 3C), we use the same 6 cpg0016 sources as before, but create a training dataset containing data from just 5 of the 6 sources. The retrieval dataset includes data from the training dataset, but also a subset of microscopy batches from the unseen source (50% of batches). We add the unseen source to the retrieval dataset because this allows us to quantify two settings for a source not included in training data: first, if the source uses the pre-trained model to compare between images generated internally, and second, if the source uses the pre-trained model to compare their images to another different source (NSB and NSS respectively in 2.3.4). The query dataset is a disjoint 50% of microscopy batches from the unseen source. Dataset stratification is randomized over 3 random seeds, and this is a source of uncertainty in our error bars (in addition to randomizing weights, where applicable for the method).

We use the Target-2 dataset to evaluate generalization to unseen compounds. We stratify the Target-2 dataset to test ID performance, and use a mixture of Target-2 and Compound plates to test OOD performance (Figure 4, with metadata about splits available in Supplementary Table A6). For the ID setting (Figure 4B), we reserve 20% of the microscopy batches as the query dataset. The remaining 80% of batches are split into training and validation datasets (holding out one batch from each source for validation), and additionally used as the retrieval dataset. For the OOD setting (Figure 4C), we train representation learning models using all batches from the Target-2 plates. To evaluate, we extend the dataset by identifying compounds from the Compound plates that elicited strong phenotypic effects across sources. For each source we ranked compounds in the Compound plates based on the replicate-averaged distance between the CellProfiler [25] image features for the compound versus features for the negative control spatially closest to the well in the plate map. We then nominated compounds in the top 10% of greatest distances for at least four sources, yielding a total of 184

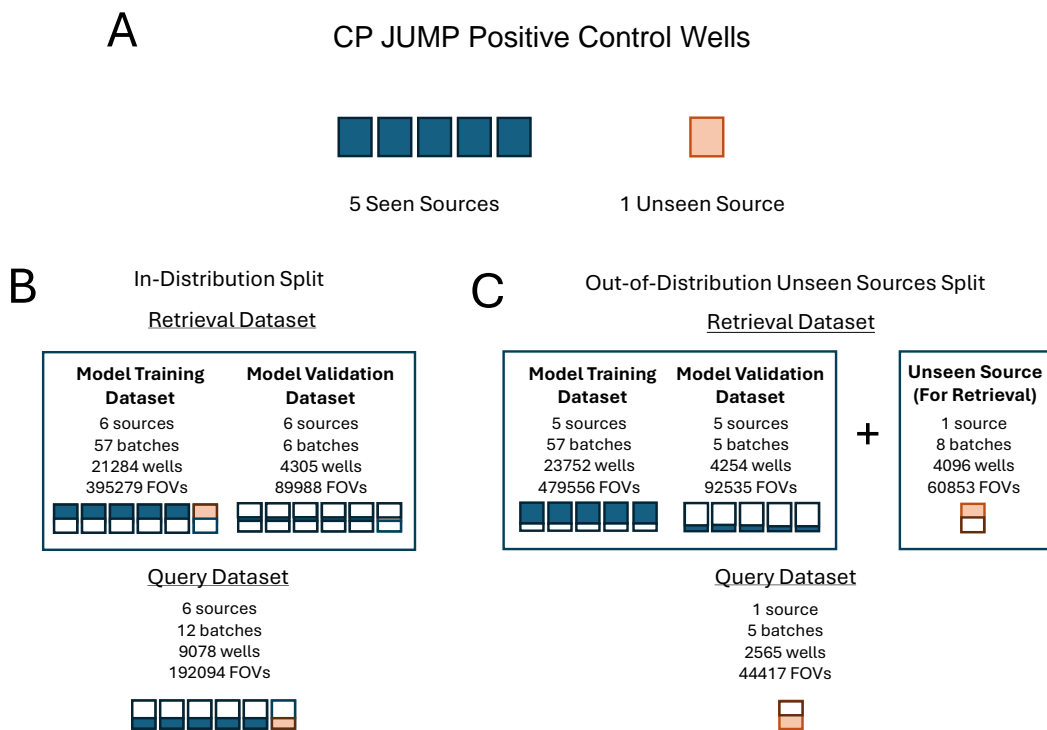


Figure 3: **Stratification of positive control wells into in-distribution and out-of-distribution datasets.** (A) POS-CTL wells from a total of six sources are used. For our out-of-distribution evaluation, five sources are designated as seen (blue boxes) during model training, and 1 source is designated as unseen (orange boxes). In panels B and C, filled parts of the boxes indicate data from each source in that split, while unfilled (white) parts of the boxes indicate held-out data (note that filled/unfilled ratios are not proportionately scaled to split ratios, and are just intended to illustrate where splits are disjoint). (B) The in-distribution evaluation trains the representation learning model on a subset of microscopy batches from all six sources, holding out one batch from each source for validation. The training and validation dataset are used as the retrieval dataset for compound-replicate matching, with unseen microscopy batches from all six sources used as the query dataset. (C) The out-of-distribution evaluation trains and validates the representation learning model on the five seen sources. For evaluation, the retrieval dataset is the training and validation data plus a subset of microscopy batches from the unseen source, and the query dataset is a disjoint subset of microscopy batches from the unseen source.

compounds. Our retrieval dataset combines the training dataset with a subset of wells (493 wells) for the unseen compounds, while the query dataset contains 368 unseen wells (2 wells per compound). This stratification scheme means that the 184 unseen compounds can be matched to 485 compounds (both the 301 compounds seen and the 184 compounds unseen during training of the representation learning model), making the compound-replicate retrieval task much more difficult and penalizing models if they overfit to compounds seen in training.

## 2.3 Implementation

### 2.3.1 Image Preprocessing

To remove systematic variation in pixel intensity from uneven illumination in the field of view (FOV), we apply illumination correction [35]. Each image was corrected by dividing all pixel intensities by the illumination correction function, calculated by taking a median filter on the average image across all FOVs in a plate. Consistent with previous representation learning studies on cell painting images [26], to reduce the disk size of the dataset, images are compressed from 16-bit TIFF files to 8-bit PNG files, rescaling each channel independently between the 0.05th and 99.95th percentile of pixels



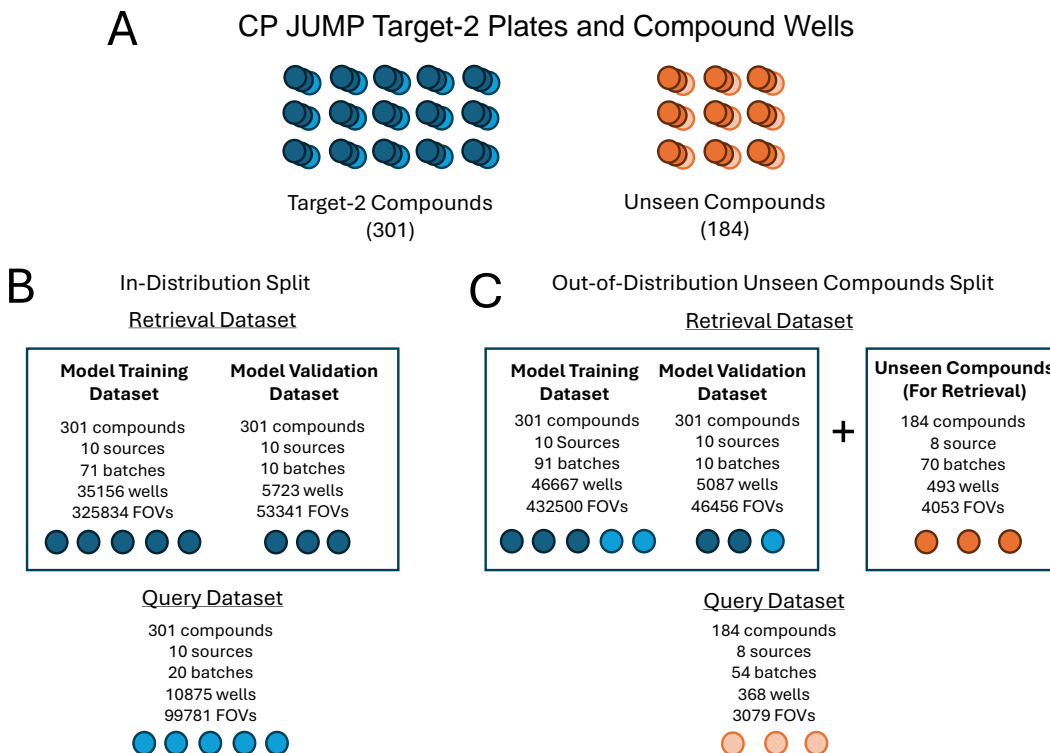


Figure 4: **Stratification of Target-2 and Compound plates into in-distribution and out-of-distribution datasets.** (A) The 301 Target-2 compounds (blue) are designated as seen compounds for training representation learning models, while 184 unseen compounds (orange) are sampled from the Compound plates and held out. (B) The in-distribution evaluation trains the representation learning model on 80% of microscopy batches from all Target-2 plates, reserving 20% of microscopy batches for the query dataset. (C) The out-of-distribution evaluation trains the representation learning model on all microscopy batches from the Target-2 plates. The training dataset is combined with 493 wells for 184 unseen compounds to form the retrieval dataset and evaluated on a query dataset of a disjoint set of 368 wells of held-out, unseen compounds from the Compound plates.

intensity-wise. To further save disk space and improve I/O speed, we take a crop of 50% of the image height and width from the center of each image. For data augmentation and to allow large batch sizes, the processed images are further re-sized to 224x224 resolution during training. Following previous works [1, 2, 37], we also evaluated the effect of spherizing representations: we first rescale features with mean absolute deviation (MAD) normalization, and then we apply spherizing, which transforms the feature space such that negative control representations have an identity covariate matrix.

### 2.3.2 Architecture and Training Details

We use ResNet101 [15], pre-trained on ImageNet, as our image encoder  $h_{img}$ , following previous works showing that ImageNet features are effective at representing phenotypic changes in morphological profiling [21, 28, 14, 11]. We replace the final fully-connected layer with a new randomly initialized layer of hidden dimension size 256 and fine-tune only this new layer, with the pre-trained encoder frozen during training. Since models pre-trained on ImageNet typically expect 3-channel inputs, we preprocess 5-channel microscopy images by converting each channel separately into a 3-channel image (as expected by the pre-trained ImageNet encoder) by duplicating the image 3 times along the channel axis. Each microscopy channel is separately preprocessed in this manner and inputted into the encoder to output an encoding of dimension 256. We concatenate the outputted encodings from the 5 original microscopy channels to obtain a final image representation with dimension  $256 \times 5 = 1280$ .

To encode chemical compounds, we represent them as ECFP4 fingerprints with a radius of 2 [33], which represents molecular structures as circular neighborhoods of atoms. The ECFP4 fingerprint

transforms a molecular structure to a bit-vector embedding which captures patterns within a two-bond radius around each atom, enabling efficient comparison of molecular structures. The compound encoder,  $\mathbf{h}_{\text{comp}}$ , is trained from scratch.  $\mathbf{h}_{\text{comp}}$  contains 4 fully-connected hidden layers of dimensionality 2048 each and interleaved with batch normalization and ReLU activations, receives as input the ECFP4 fingerprint, and outputs a molecular encoding of dimension 2048. We also tested starting from a pre-trained 3D molecular encoder, UniMol [38], but observed in initial experiments that this did not improve performance.

The fusion module accepts as input a concatenation of a negative control image embedding and a molecule embedding. The model is implemented as a two-layer multi-layer perceptron with leaky-ReLU activations. Finally, all image representations (i.e. both representations of real images and counterfactual representations) are passed through a projection head  $g$ , also implemented as a two-layer multi-layer perceptron with leaky-ReLU activations. Together, these components (the image encoder  $\mathbf{h}_{\text{img}}$ , the chemical compound encoder  $\mathbf{h}_{\text{comp}}$ , the fusion module  $F$ , and the projection head  $g$ ) are combined into the overall MICON framework (Figure 1). The entire model is optimized end-to-end with the overall MICON loss, with the exception of the frozen components of the image encoder.

We train using the AdamW optimizer [19] using a ReduceLRonPlateau learning rate scheduler using batch size 64 for 30 epochs on two NVIDIA A100-40G graphic cards. We oversample negative controls to form half of the training batch for our POS-CTL models and one eighth of the training batch for our Target-2 models. We perform a linear warm-up for 2000 steps. All models are trained 3 times from random seeds. We save checkpoints at every 2000 steps, and use the best-performing checkpoint on the validation dataset for testing. Detailed hyper-parameters and architectural details can be found in Table A7 in the supplementary materials.

### 2.3.3 Baselines and Ablations

We compare MICON to the following baselines and ablations: hand-crafted, image-based features (“CellProfiler”); an image-only, self-supervised contrastive learning model (“SimCLR”); and a CLIP-based multi-modal model that aligns image and chemical compound representations (“CLIP”).

CellProfiler [25] features – which are hand-designed, image-based texture, shape, and intensity features – were provided by and downloaded from the JUMP-CP dataset [8]. Models trained using SimCLR [9] provided an image-only, self-supervised contrastive learning baseline to validate our strategy of integrating chemical compound information in a multi-modal framework. To specifically evaluate the counterfactual aspect of the MICON framework, we trained multi-modal baseline models using CLIP [31], which directly aligns image and chemical compound representations in a shared embedding space. A CLIP-based approach for multimodal learning between microscopy images and chemical compounds was previously proposed by CLOOME [34] and extended in MolPhenix [13]. As these works use different architectures, datasets, and pre-trained models, they do not provide appropriate baseline controls to MICON. We train a CLIP baseline model using the same dataset and encoder architectures as MICON to enable direct comparison of the method itself, instead of transferring these models, which could result in disparities in performance from these other factors. Thus, we refer to the resulting baseline model as “CLIP.”

Both the SimCLR and CLIP models use the same architectures, dataset, and stopping criterion as MICON in Section 2.3.2, when applicable to the model (i.e., SimCLR and CLIP also use ResNet101 pre-trained on ImageNet, while CLIP also uses our ECFP4-based compound encoder trained from scratch). All models are trained 3 times with distinct random seeds.

### 2.3.4 Evaluation Implementation

To implement compound-replicate retrieval, we identify the nearest neighbor in the retrieval dataset, using the cosine distance of the representation, for each well in the query dataset. We report the accuracy of this retrieval, defined as the fraction of wells where the nearest well in the retrieval dataset is treated with the same perturbation. As each well is typically imaged with multiple FOVs, we average the representations of all FOVs to form a well-level representation. To test if representations are robust to microscopy batch effects caused by differences in microscopy batch and source, we further restrict matching to the nearest neighbor in a different microscopy batch (Not in Same Batch - NSB) or source (Not in Same Source - NSS).

### 2.3.5 Code and Data Availability

Code to reproduce our analyses and model is available at [github.com/microsoft/MICON](https://github.com/microsoft/MICON). Model weights and representations from our models are available at <https://www.dropbox.com/scl/fo/93yi5kr2878xznihjcf9w/APySE0JdKPbcM25e2UGF3cw?rlkey=casz2x8z3dwxgg99yom8ip1jb&st=brziiel2&dl=0>. As the image datasets are readily available from the JUMP Cell Painting Consortium [8], and too large to re-upload, we instead provide scripts to reproduce our splits and preprocessing.

## 3 Results

To validate MICON, we ran 8 experiments that reflect different challenges for morphological profiling, including integration across batches and sources as well as generalization to microscopy batch effects and perturbations unseen in training (Figure 5; Supplementary Tables A1,A2). We benchmarked MICON against baselines and ablated the counterfactual PaCLR loss – and therefore information about chemical structures – to evaluate how integration of chemical compounds improves representation learning in morphological profiling. Our results demonstrate that our full MICON method using the counterfactual PaCLR loss results in a sizable improvement over the CellProfiler, SIMCLR, and CLIP baselines. While performance improvements over using just the PaCLR loss alone were smaller, and thus not always statistically significant for individual experiments, pooling experiments indicated that the counterfactual PAC loss significantly improves performance (F-ratio value of 9.249, p-value 0.0228 with a one-way repeated measures ANOVA), suggesting that our counterfactual integration of chemical compounds during training is effective at improving representations of microscopy images. In subsequent sections, we expand on the results of each experiment.

### 3.1 MICON improves representations of images

We first trained MICON and the baseline models on the ID (in-distribution) training dataset of the POS-CTL wells, on a total of 21,284 wells from 6 sources (Figure 3B). The positive control wells represent 8 compounds nominated to be morphologically distinct from DMSO and each other [8]. We used this positive control dataset to measure if representations can identify reproducible effects of chemical compounds that induce relatively strong phenotypic effects across increasing batch effects. Using the trained models, as well as CellProfiler features, we extracted representations for 9,078 unseen wells (Figure 3B; a subset of these representations are shown as a UMAP in Supplementary Figure A1) and measured compound-replicate retrieval accuracy, specifically how frequently the nearest-retrieved NSB (not in same batch) and NSS (not in same source) neighbor was treated with the same chemical compound (Figure 5A; Supplementary Table A1). CellProfiler features, the common-practice standard in the field, yielded a 1-NN NSB accuracy of 36.56% and a 1-NN NSS accuracy of 9.32% on the positive control test dataset, with an accuracy of 9.32% following the expected 12.5% accuracy of random guessing across 8 compounds. In contrast, MICON achieved a 1-NN NSB accuracy of 62.24% and a 1-NN NSS accuracy of 28.43%, significantly outperforming both CellProfiler features as well as unimodal (SimCLR, 37.77% 1-NN NSB and 16.56% 1-NN NSS accuracies) and multi-modal (CLIP, 34.33% 1-NN NSB and 12.16% 1-NN NSS accuracies) self-supervised learning methods (Figure 5A; Supplementary Table A1).

We then asked whether these performance gains were due to MICON’s multimodal integration of chemical structures or if they could be fully attributed to the PaCLR component, which operates exclusively on images. To test this, we ablated the counterfactual PaCLR component of the MICON loss, which is the only component that integrates chemical compounds, and trained a model using just the PaCLR loss. While this ablated model underperformed the full MICON model, it still outperformed the baselines, achieving a 1-NN NSB accuracy of 56.57% and a 1-NN NSS accuracy of 25.21% (Figure 5A; Supplementary Table A1). Together, these results suggest that, while the majority of MICON’s strong performance is driven by the PaCLR loss, the integration of chemical compound information further improves the quality of its representations.

### 3.2 MICON generalizes to unseen sources

We next sought to understand if MICON generalized to sources unseen in training. Many representation learning methods are designed to learn representations invariant to microscopy batch effects.

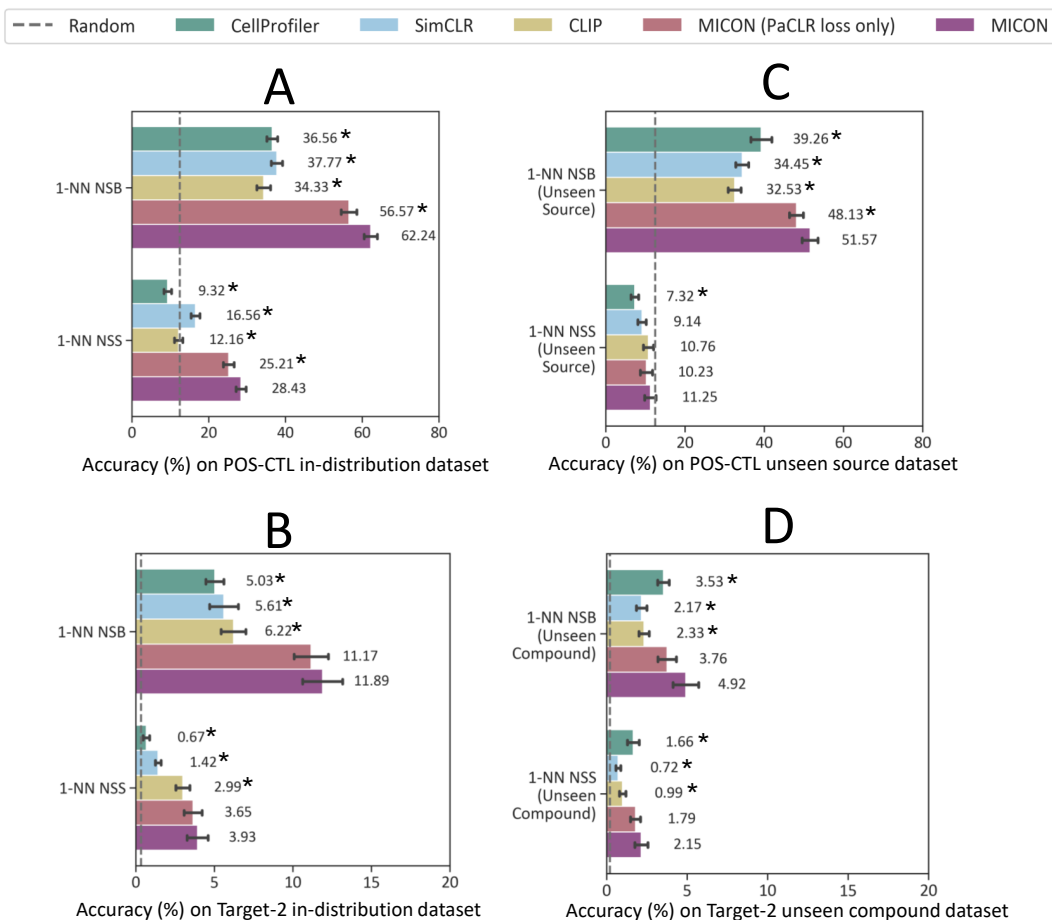


**Figure 5: Compound-replicate retrieval accuracy for representation learning methods across evaluation settings.** Retrieval accuracies on the (A) POS-CTL ID query dataset, (B) Target-2 ID query dataset, (C) POS-CTL OOD query dataset (unseen source), and (D) Target-2 OOD query dataset (unseen compounds). NSB designates retrieval of the nearest neighbor not in the same batch; NSS designates retrieval of the nearest neighbor not in the same source.  $n=3$  models trained and evaluated with different dataset stratifications and different random seeds; the mean accuracy is labeled, and the error bars represent standard deviation. Asterisk indicates that MICON significantly outperforms the baseline, defined as  $p < 0.05$  on an unpaired one-tailed t-test with performance across the  $n=3$  random seeds as trials.

This is true not just of MICON, whose contrastive method minimizes distances between images treated with the same perturbation across different sources, but also CLIP, which maps images treated with the same perturbation across sources to the same chemical compound representation. Hence, a major question with these representation learning methods is if these learned invariances generalize, or if they are overfit to sources seen during training.

To assess generalization to unseen sources, we designed an OOD (out-of-distribution) experiment using the POS-CTL wells, in which the training dataset consists of 5 seen sources and the query dataset consists wholly of a sixth source unseen during training of the representation learning model (Figure 3C). For each representation learning method, we evaluated compound-replicate retrieval performance on the unseen source test dataset and found that all representation learning methods dropped in performance when sources are unseen in training (Figure 5C; Supplementary Table A1). Notably, in the NSB setting, SimCLR (34.45%) and CLIP (32.53%) no longer outperformed CellProfiler (39.26%), suggesting that performance above CellProfiler may be because of overfitting to seen sources. However, MICON (51.57%) still significantly outperformed CellProfiler, SimCLR, and CLIP, indicating MICON’s capacity to generalize to unseen sources. In the NSS setting, MICON’s

performance (11.25%) was not significantly better than that of SimCLR (9.14%) or CLIP (10.76%), although MICON was significantly better than CellProfiler (7.32%). We note that the unseen source NSS experiment is the only where all methods underperformed random guessing, suggesting that comparing data across sources, if the source is unseen during training of representation learning models, remains an unsolved problem.

### 3.3 MICON demonstrates robust performance over larger compound datasets with unseen compounds

While our previous experiments focused on data representing just 8 chemical compound treatments, most morphological profiling experiments assay a greater number of perturbations. Therefore, we next sought to evaluate the performance of MICON when trained on datasets with a larger number of chemical compounds. We trained a MICON model on a total of 35,156 wells subsetted from the Target-2 plates, which image 301 perturbations replicated across all sources (Figure 4B; a subset of these representations are shown as a UMAP in Supplementary Figure A2).

As with our POS-CTL well experiments, we evaluated NSB and NSS compound-replicate retrieval accuracy on an unseen query dataset. Due to the greater number of chemical compounds, this task becomes much more challenging – the accuracy expected from random guessing is 0.33% (1 in 301). The CellProfiler, SimCLR, and CLIP baselines exhibited performance ranging from 5.03 – 6.22% for NSB accuracy and from 0.67 – 2.99% for NSS accuracy, while MICON significantly improved on these baselines, providing 11.89% NSB accuracy and 3.93% NSS accuracy (Figure 5B). We show examples of the images retrieved by MICON versus CellProfiler in Supplementary Figure A3.

One limitation of our compound-replicate evaluation is that representation learning strategies that incorporate information about chemical compounds (i.e., both MICON and CLIP) may potentially overfit to compounds seen during training, which may result in a poorer representation of phenotypes induced by new, unseen compounds. To test this, we constructed an independent, OOD test dataset of wells treated with 184 compounds unseen during training (Figure 4C). We sampled these wells from the Compound plates of the JUMP-CP cpg0016 dataset and evaluated whether models trained on the Target-2 plates could still identify reproducible effects in images across these unseen compounds. In the retrieval dataset, we still included the 301 compounds seen during training of representation learning models, in addition to the 184 new unseen compounds, but the query set was comprised of only the 184 new compounds (Figure 4C). This scheme not only increases the difficulty of the retrieval task, because more perturbation labels are possible, but should also penalize representation learning models that overfit to compounds seen during training, because these are included as possible labels for predicting the compound treatment of new, unseen compounds.

We observed that the baseline representation learning methods, SimCLR and CLIP, were not robust when evaluated on compounds unseen in the training dataset, resulting in accuracies well below that of CellProfiler features, despite being originally superior on seen compounds (Figure 5D). While CellProfiler features had an NSB accuracy of 3.53% and an NSS of 1.66%, SimCLR resulted in an NSB of 2.17% and an NSS of 0.72%, while CLIP had an NSB of 2.33% and an NSS of 0.99%. In contrast, MICON performed significantly better than the CellProfiler, SimCLR, and CLIP baselines on unseen compounds, achieving an NSB of 4.92% and an NSS of 2.15% (Figure 5D; Table A2). These results demonstrate that incorporating information about perturbations into representation learning yields improvements in image representations that generalize to new, unseen perturbations.

### 3.4 MICON benefits from microscopy batch effect correction

While our evaluations thus far used the raw representations from MICON and baselines, in practice, batch effect correction is often applied *post hoc* to representations from morphological profiling. One common transformation is to spherize representations for each plate such that the negative control representations have an identity covariate matrix [1, 37]. This transformation assumes access to a large number of positive controls per plate, which may not always hold true (i.e., if a lab is not performing high-throughput experiments), so we did not apply it as default in our previous experiments. However, in most high-throughput experiments, the assumption does hold, and spherizing is effective at compensating for microscopy batch effects.

We therefore assessed the impact of microscopy batch effect correction on MICON representations relative to the baseline methods by conducting compound-replicate retrieval, but with spherized

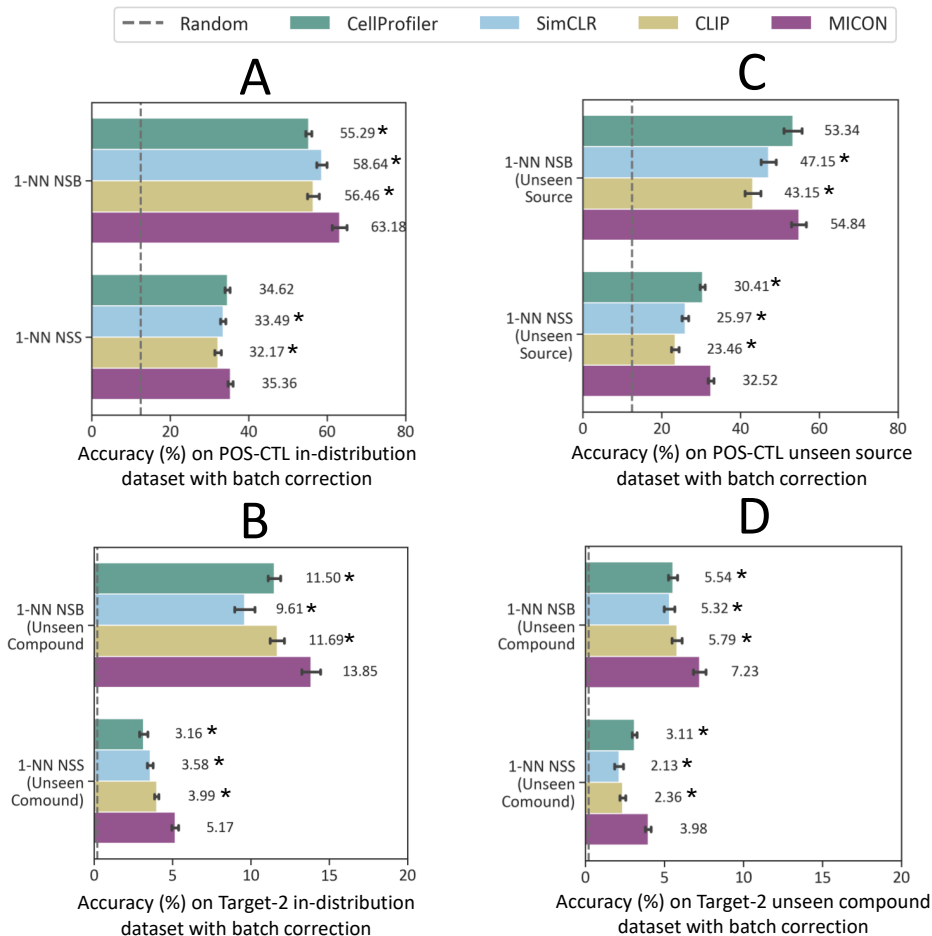


**Figure 6: Compound-replicate retrieval accuracy for representation learning methods across evaluation settings, when microscopy batch effect correction is applied via spherizing.** Retrieval accuracies on the (A) POS-CTL ID query dataset, (B) Target-2 ID query dataset, (C) POS-CTL OOD query dataset (unseen source), and (D) Target-2 OOD query dataset (unseen compounds). NSB designates retrieval of the nearest neighbor not in the same batch; NSS designates retrieval of the nearest neighbor not in the same source.  $n=3$  models trained and evaluated with different dataset stratifications and different random seeds; the mean accuracy is labeled, and the error bars represent standard deviation. Asterisk indicates that MICON significantly outperforms the baseline, defined as  $p < 0.05$  on an unpaired one-tailed t-test with performance across the  $n=3$  random seeds as trials.

representations, across the 8 evaluation settings (Figure 6). Spherizing substantially improved the performance of all representations evaluated. Interestingly, across almost all experiments, SimCLR and CLIP now underperformed or performed similarly to CellProfiler. These observations suggest that the previously observed improvements from the SimCLR and CLIP baselines without batch effect correction (Figure 5) may be primarily driven by an inherent robustness to microscopy batch effects in the feature representations, and that this difference is compensated for when CellProfiler features are post-processed with batch effect correction (Figure 6). Critically, MICON representations still significantly outperformed SimCLR and CLIP representations in all experiments, and were significantly better or similar to CellProfiler features in all experiments (significantly better in 6 of 8 settings), suggesting that MICON performance is driven by superior recognition of phenotypic effects, not just robustness to microscopy batch effects (Figure 6).

POS-CTL	ID NSB	ID NSS	UNSEEN SOURCES NSB	UNSEEN SOURCES NSS
RANDOM			12.50	
MICON (REAL IMAGES)	63.18 $\pm$ 3.53	35.36 $\pm$ 3.21	54.84 $\pm$ 1.94	32.52 $\pm$ 2.32
MICON (GENERATED)	54.75 $\pm$ 3.21	26.14 $\pm$ 3.37	47.26 $\pm$ 3.46	25.93 $\pm$ 2.02
TGT-2	ID NSB	ID NSS	UNSEEN COMPOUNDS NSB	UNSEEN COMPOUNDS NSS
RANDOM			0.33	
MICON (REAL IMAGES)	13.85 $\pm$ 2.79	5.17 $\pm$ 1.28	7.23 $\pm$ 1.73	3.98 $\pm$ 0.67
MICON (GENERATED)	13.64 $\pm$ 2.03	4.76 $\pm$ 0.93	2.54 $\pm$ 0.58	1.07 $\pm$ 0.21

Table 1: **Nearest neighbor retrieval accuracies (%) using real perturbation representations vs. generated counterfactual representations, across evaluation settings.** NSB designates retrieval of the nearest neighbor not in the same batch; NSS designates retrieval of the nearest neighbor not in the same source. Error represents the standard deviation across 3 independent replicates.

### 3.5 MICON can synthesize phenotypic effects of unseen compounds

Together, our previous experiments demonstrate that the MICON objective improves image representation learning, as assessed by compound-replicate matching. The counterfactual PaCLR component of the objective means that MICON models should additionally be able to predict the phenotypic effect of compound perturbations. As a proof-of-concept test of this capability, we assessed how frequently the counterfactual representations from MICON models yield retrieval of a representation from a real image of cells perturbed with the same compound. We replicated each of the previous retrieval experiments, except using counterfactual representations instead of real ones. For each real perturbation representation originally used in compound-replicate matching, we replaced that representation with a counterfactual representation, using the spatially nearest negative control on the plate map as the basis for generation. This set-up enabled direct comparison of retrieval performance with counterfactual representations versus performance with the real perturbation representations, which serves as an upper bound on performance.

We observed that, for seen compounds, retrieval with the counterfactual representations only slightly declined in performance compared to with the real perturbation representations (Table 1), even when retrieving across sources and with unseen sources. For compounds unseen in training, the decline in performance was more substantial, but, notably, performance with counterfactual representations was still several folds higher than random guessing accuracy. These results suggest that MICON’s counterfactual generations capture phenotypic effects of compounds seen in training, with some ability to capture the phenotypic impact of completely unseen compounds.

## 4 Discussion

In this work, we introduce MICON, a molecular-image representation learning method for morphological profiling. MICON integrates two losses during training using contrastive learning: a perturbation-aware contrastive (PAC) loss that encourages representations of real images to be invariant to microscopy batch effects, and a counterfactual PaCLR loss that aligns representations of synthetic images generated using chemical compound information with those of real images of cells treated with the compound. Both components substantially advance representation learning. Even stand-alone, MICON’s perturbation-aware contrastive loss enables identification of reproducible phenotypic effects of compounds under batch effects, achieving improvements over both CellProfiler features and representation learning baselines like SimCLR. We attribute this to the use of perturbation and microscopy batch metadata to mine both positive and negative samples for representation learning.

We show that MICON’s counterfactual PaCLR loss further improves performance in identifying phenotypic effects in images relative to models trained with just the PaCLR loss. This result demonstrates that integrating multimodal information about perturbation treatments can improve unimodal representations of images, establishing directions for future morphological profiling methods. Towards this, we also demonstrate that *how* images and chemical compounds should be integrated is crucial. MICON models chemical compounds as a counterfactual transformation of images, and this approach strongly outperforms the CLIP-like strategy of directly aligning images and chemical compounds.

In order to benchmark our modeling contribution, we also made substantial strides in evaluation. Taking advantage of the large-scale and multi-source nature of the JUMP-CP dataset, we designed evaluation splits that allow us to assess if morphological profiling methods can maintain performance when comparing images from different data-generating sources and when sources or compounds are unseen during representation learning (Figure 3, 4). This evaluation framework is more comprehensive than those used to evaluate previous representation learning models, which often use only a dataset collected by a single source and usually do not stratify compounds such that some are unseen in representation learning [36, 34, 12]. Even when methods train on multi-source data, they do not evaluate the ability to identify reproducible phenotypes across different sources [18], which we argue is critical for robust representation learning. Our evaluation exposes that some representation learning methods previously reported to be effective for morphological profiling may be overfitting and thus overestimating their performance. For example, while SimCLR outperforms CellProfiler features when representing seen compounds, it underperforms CellProfiler on compounds unseen during training. In contrast, MICON is robust and demonstrates consistent improvements over both CellProfiler and baseline representation learning methods across all scenarios evaluated, even when compounds are unseen in training and even when considering more challenging batch effects like differing imaging sources.

Future work should explore if MICON stays robust when deployed on larger and less curated datasets. In this work, we focused on a small number of perturbations that were more likely to have strong phenotypic effects. However, drug screening experiments are usually systematic in nature and will thus include many compounds that elicit minimal phenotypic impact on cells relative to negative controls. As MICON’s PaCLR loss forces the model to distinguish compound-treated images from negative controls, it is not clear if scaling the number of compounds in the training dataset will adversely affect learning. Future work should analyze the trade-off between indiscriminately scaling the number of images and/or compounds (which may imbalance the distribution of phenotypes) versus downsampling datasets to just the stronger phenotypic effects. Second, in this work, we focused on the POS-CTL wells and the Target-2 plates of cpg0016, which are reproduced multiple times by multiple sources. In contrast, some compounds in cpg0016 are only assayed by a subset of sources and once by each source. This reflects another trade-off in training data that should be explored in future work: it is unclear if focusing training on a small subset of well-reproduced compounds can explain some of the effectiveness of MICON or if expanding the number of compounds at the cost of less coverage across sources would further improve our method.

Extending MICON to additional perturbation modalities, such as genetic or environmental perturbations, could similarly model them as treatments that induce a counterfactual transformation of images. MICON’s counterfactual framework enables prediction of representations and, hence, phenotypic effects of unseen compounds, with observed performance measuring above random chance. While optimizing this capability is beyond the scope of our work, as our current method is limited by the use of a relatively small number of perturbations during training, the ability to predict the phenotypic effects of perturbations prior to experimentation could make high-throughput drug screens more resource efficient by triaging compounds that are more likely to be effective. Towards this capability, our proof-of-concept demonstrates generation is possible directly in a learned latent space, paralleling similar work with conditional generative models [27] that produce synthetic images that reflect perturbation phenotypes. In sum, through multimodal modeling of perturbations and images in a counterfactual framework, MICON provides a new direction for representation learning in morphological profiling, paving the way for new methods that explicitly leverage the multimodal nature of microscopy screens.

## 5 Declaration of Interests

N.T, L.M, D.A.M, A.P.M, and A.X.L are employees of and hold equity in Microsoft.

## References

- [1] D. M. Ando, C. Y. McLean, and M. Berndl. Improving phenotypic measurements in high-content imaging screens. *BioRxiv*, page 161422, 2017.
- [2] J. Arevalo, E. Su, J. D. Ewald, R. van Dijk, A. E. Carpenter, and S. Singh. Evaluating batch correction methods for image-based cell profiling. *Nature Communications*, 15(1):6516, 2024.



- [3] M.-A. Bray, S. Singh, H. Han, C. T. Davis, B. Borgeson, C. Hartland, M. Kost-Alimova, S. M. Gustafsdottir, C. C. Gibson, and A. E. Carpenter. Cell painting, a high-content image-based assay for morphological profiling using multiplexed fluorescent dyes. *Nature protocols*, 11(9): 1757–1774, 2016.
- [4] J. C. Caicedo, S. Cooper, F. Heigwer, S. Warchal, P. Qiu, C. Molnar, A. S. Vasilevich, J. D. Barry, H. S. Bansal, O. Kraus, et al. Data-analysis strategies for image-based cell profiling. *Nature methods*, 14(9):849–863, 2017.
- [5] J. C. Caicedo, C. McQuin, A. Goodman, S. Singh, and A. E. Carpenter. Weakly supervised learning of single-cell feature embeddings. In *Proceedings of the IEEE Conference on Computer Vision and Pattern Recognition*, pages 9309–9318, 2018.
- [6] M. Caron, H. Touvron, I. Misra, H. Jégou, J. Mairal, P. Bojanowski, and A. Joulin. Emerging properties in self-supervised vision transformers. In *Proceedings of the IEEE/CVF international conference on computer vision*, pages 9650–9660, 2021.
- [7] A. E. Carpenter, T. R. Jones, M. R. Lamprecht, C. Clarke, I. H. Kang, O. Friman, D. A. Guertin, J. H. Chang, R. A. Lindquist, J. Moffat, et al. Cellprofiler: image analysis software for identifying and quantifying cell phenotypes. *Genome biology*, 7:1–11, 2006.
- [8] S. N. Chandrasekaran, J. Ackerman, E. Alix, D. M. Ando, J. Arevalo, M. Bennion, N. Boisseau, A. Borowa, J. D. Boyd, L. Brino, et al. Jump cell painting dataset: morphological impact of 136,000 chemical and genetic perturbations. *bioRxiv*, pages 2023–03, 2023.
- [9] T. Chen, S. Kornblith, M. Norouzi, and G. Hinton. A simple framework for contrastive learning of visual representations. In *International conference on machine learning*, pages 1597–1607. PMLR, 2020.
- [10] Z. S. Chen, C. Pham, S. Wang, M. Doron, N. Moshkov, B. Plummer, and J. C. Caicedo. Chammi: A benchmark for channel-adaptive models in microscopy imaging. *Advances in Neural Information Processing Systems*, 36, 2024.
- [11] J. O. Cross-Zamirski, G. Williams, E. Mouchet, C.-B. Schönlieb, R. Turkki, and Y. Wang. Self-supervised learning of phenotypic representations from cell images with weak labels. *arXiv preprint arXiv:2209.07819*, 2022.
- [12] M. Doron, T. Moutakanni, Z. S. Chen, N. Moshkov, M. Caron, H. Touvron, P. Bojanowski, W. M. Pernice, and J. C. Caicedo. Unbiased single-cell morphology with self-supervised vision transformers. *bioRxiv*, 2023.
- [13] P. Fradkin, P. Azadi, K. Suri, F. Wenkel, A. Bashashati, M. Sypetkowski, and D. Beaini. How molecules impact cells: Unlocking contrastive phenomolecular retrieval. *arXiv preprint arXiv:2409.08302*, 2024.
- [14] W. J. Godinez, I. Hossain, S. E. Lazic, J. W. Davies, and X. Zhang. A multi-scale convolutional neural network for phenotyping high-content cellular images. *Bioinformatics*, 33(13):2010–2019, 2017.
- [15] K. He, X. Zhang, S. Ren, and J. Sun. Deep residual learning for image recognition. In *Proceedings of the IEEE conference on computer vision and pattern recognition*, pages 770–778, 2016.
- [16] K. He, X. Chen, S. Xie, Y. Li, P. Dollár, and R. Girshick. Masked autoencoders are scalable vision learners. In *Proceedings of the IEEE/CVF conference on computer vision and pattern recognition*, pages 16000–16009, 2022.
- [17] R. Janssens, X. Zhang, A. Kauffmann, A. de Weck, and E. Y. Durand. Fully unsupervised deep mode of action learning for phenotyping high-content cellular images. *Bioinformatics*, 37(23): 4548–4555, 2021.
- [18] V. Kim, N. Adaloglou, M. Osterland, F. M. Morelli, M. Halawa, T. König, D. Gnutt, and P. A. M. Zapata. Self-supervision advances morphological profiling by unlocking powerful image representations. *BioRxiv*, pages 2023–04, 2023.

- [19] D. P. Kingma. Adam: A method for stochastic optimization. *arXiv preprint arXiv:1412.6980*, 2014.
- [20] O. Kraus, K. Kenyon-Dean, S. Saberian, M. Fallah, P. McLean, J. Leung, V. Sharma, A. Khan, J. Balakrishnan, S. Celik, et al. Masked autoencoders for microscopy are scalable learners of cellular biology. In *Proceedings of the IEEE/CVF Conference on Computer Vision and Pattern Recognition*, pages 11757–11768, 2024.
- [21] O. Z. Kraus, J. L. Ba, and B. J. Frey. Classifying and segmenting microscopy images with deep multiple instance learning. *Bioinformatics*, 32(12):i52–i59, 2016.
- [22] A. Lin and A. Lu. Incorporating knowledge of plates in batch normalization improves generalization of deep learning for microscopy images. In *Machine Learning in Computational Biology*, pages 74–93. PMLR, 2022.
- [23] S. Lin, K. Schorpp, I. Rothenaigner, and K. Hadian. Image-based high-content screening in drug discovery. *Drug discovery today*, 25(8):1348–1361, 2020.
- [24] V. Ljosa, P. D. Caie, R. Ter Horst, K. L. Sokolnicki, E. L. Jenkins, S. Daya, M. E. Roberts, T. R. Jones, S. Singh, A. Genovesio, et al. Comparison of methods for image-based profiling of cellular morphological responses to small-molecule treatment. *Journal of biomolecular screening*, 18(10):1321–1329, 2013.
- [25] C. McQuin, A. Goodman, V. Chernyshev, L. Kametsky, B. A. Cimini, K. W. Karhohs, M. Doan, L. Ding, S. M. Rafelski, D. Thirstrup, et al. Cellprofiler 3.0: Next-generation image processing for biology. *PLoS biology*, 16(7):e2005970, 2018.
- [26] N. Moshkov, M. Bornholdt, S. Benoit, M. Smith, C. McQuin, A. Goodman, R. A. Senft, Y. Han, M. Babadi, P. Horvath, et al. Learning representations for image-based profiling of perturbations. *Nature Communications*, 15(1):1594, 2024.
- [27] A. Palma, F. J. Theis, and M. Lotfollahi. Predicting cell morphological responses to perturbations using generative modeling. *bioRxiv*, pages 2023–07, 2023.
- [28] N. Pawlowski, J. C. Caicedo, S. Singh, A. E. Carpenter, and A. Storkey. Automating morphological profiling with generic deep convolutional networks. *BioRxiv*, page 085118, 2016.
- [29] A. Perakis, A. Gorji, S. Jain, K. Chaitanya, S. Rizza, and E. Konukoglu. Contrastive learning of single-cell phenotypic representations for treatment classification. In *Machine Learning in Medical Imaging: 12th International Workshop, MLMI 2021, Held in Conjunction with MICCAI 2021, Strasbourg, France, September 27, 2021, Proceedings 12*, pages 565–575. Springer, 2021.
- [30] A. Pratapa, M. Doron, and J. C. Caicedo. Image-based cell phenotyping with deep learning. *Current opinion in chemical biology*, 65:9–17, 2021.
- [31] A. Radford, J. W. Kim, C. Hallacy, A. Ramesh, G. Goh, S. Agarwal, G. Sastry, A. Askell, P. Mishkin, J. Clark, et al. Learning transferable visual models from natural language supervision. In *International conference on machine learning*, pages 8748–8763. PMLR, 2021.
- [32] V. Rani, S. T. Nabi, M. Kumar, A. Mittal, and K. Kumar. Self-supervised learning: A succinct review. *Archives of Computational Methods in Engineering*, 30(4):2761–2775, 2023.
- [33] D. Rogers and M. Hahn. Extended-connectivity fingerprints. *Journal of chemical information and modeling*, 50(5):742–754, 2010.
- [34] A. Sanchez-Fernandez, E. Rumetshofer, S. Hochreiter, and G. Klambauer. Cloome: contrastive learning unlocks bioimaging databases for queries with chemical structures. *Nature Communications*, 14(1):7339, 2023.
- [35] S. Singh, M.-A. Bray, T. Jones, and A. Carpenter. Pipeline for illumination correction of images for high-throughput microscopy. *Journal of microscopy*, 256(3):231–236, 2014.
- [36] Q. Tang, R. Ratnayake, G. Seabra, Z. Jiang, R. Fang, L. Cui, Y. Ding, T. Kahveci, J. Bian, C. Li, et al. Morphological profiling for drug discovery in the era of deep learning. *Briefings in Bioinformatics*, 25(4), 2024.

- [37] G. P. Way, T. Natoli, A. Adeboye, L. Litichevskiy, A. Yang, X. Lu, J. C. Caicedo, B. A. Cimini, K. Karhohs, D. J. Logan, et al. Morphology and gene expression profiling provide complementary information for mapping cell state. *Cell systems*, 13(11):911–923, 2022.
- [38] G. Zhou, Z. Gao, Q. Ding, H. Zheng, H. Xu, Z. Wei, L. Zhang, and G. Ke. Uni-mol: A universal 3d molecular representation learning framework. 2023.
- [39] S. Ziegler, S. Sievers, and H. Waldmann. Morphological profiling of small molecules. *Cell chemical biology*, 28(3):300–319, 2021.

## A Supplementary Information

Table A1: **Top-1 Not-Same-Batch (NSB) / Not-Same-Source (NSS) 1-NN Retrieval Accuracy across the 4 benchmarking settings for the POS-CTL test datasets**, identical to the results in Figure 5 and reproduced in numerical form for reproducibility purposes. Error bars represent the standard deviation across  $n=3$  replicates with random seeds. Asterisk indicates that MICON significantly outperforms the baseline, defined as  $p < 0.05$  on an unpaired one-tailed t-test with performance across the  $n=3$  random seeds as trials.

POS-CTL(ID)	1-NN NSB	1-NN NSS	1-NN NSB (UNSEEN SOURCE)	1-NN NSS (UNSEEN SOURCE)
RANDOM CHANCE CELLPROFILER	36.56 ± 1.16*	9.32 ± 0.79*	12.50 39.26 ± 2.17*	7.42 ± 0.79*
SIMCLR CLIP	37.77 ± 1.18* 34.33 ± 1.46*	16.56 ± 0.95* 12.16 ± 0.88*	34.45 ± 1.32* 32.53 ± 1.34*	9.12 ± 0.86 10.76 ± 1.04
MICON (BAC LOSS ONLY) MICON	56.57 ± 1.65* <b>62.24 ± 1.41</b>	25.21 ± 1.16* <b>28.43 ± 1.05</b>	48.13 ± 1.41* <b>51.57 ± 1.66</b>	10.23 ± 1.26 <b>11.25 ± 1.18</b>

Table A2: **Top-1 Not-Same-Batch (NSB) / Not-Same-Source (NSS) 1-NN retrieval accuracy across the 4 benchmarking settings for the TGT2 test datasets**, identical to the results in Figure 5 and reproduced in numerical form for reproducibility purposes. Error bars represent the standard deviation across  $n=3$  replicates with random seeds. Asterisk indicates that MICON significantly outperforms the baseline, defined as  $p < 0.05$  on an unpaired one-tailed t-test with performance across the  $n=3$  random seeds as trials.

TGT-2 (ID)	1-NN NSB (ID)	1-NN NSS (ID)	1-NN NSB (UNSEEN COMPOUND)	1-NN NSS (UNSEEN COMPOUND)
RANDOM CHANCE CELLPROFILER	5.03 ± 0.43*	0.33 0.67 ± 0.17*	3.53 ± 0.29*	0.21 1.66* ± 0.29
SIMCLR CLIP	5.61 ± 0.75* 6.22 ± 0.64*	1.42 ± 0.15* 2.99 ± 0.36*	2.17 ± 0.27* 2.33 ± 0.26*	0.42 ± 0.12* 0.99 ± 0.16*
MICON (BAC LOSS ONLY) MICON	11.17 ± 0.89 <b>11.89 ± 1.04</b>	3.65 ± 0.47 <b>3.93 ± 0.55</b>	3.76 ± 0.43 <b>4.92 ± 0.65</b>	1.79 ± 0.25 <b>2.15 ± 0.33</b>

Table A3: **Top-1 Not-Same-Batch (NSB) / Not-Same-Source (NSS) 1-NN Retrieval Accuracy across the 4 benchmarking settings the POS-CTL test datasets after batch correction post-processing**, identical to the results in Figure 6 and reproduced in numerical form for reproducibility purposes. Error bars represent the standard deviation across  $n=3$  replicates with random seeds. Asterisk indicates that MICON significantly outperforms the baseline, defined as  $p < 0.05$  on an unpaired one-tailed t-test with performance across the  $n=3$  random seeds as trials.

POS-CTL(ID)	1-NN NSB	1-NN NSS	1-NN NSB (UNSEEN SOURCE)	1-NN NSS (UNSEEN SOURCE)
RANDOM CHANCE CELLPROFILER	55.29 ± 0.63*	34.62 ± 0.52	12.50 53.34 ± 1.87	30.41 ± 0.52*
SIMCLR CLIP	58.64 ± 1.06* 56.46 ± 1.22*	33.49 ± 0.54* 32.17 ± 0.68*	47.15 ± 1.55* 43.15 ± 1.63*	25.97 ± 0.68* 23.46 ± 0.78*
MICON	<b>63.18 ± 1.53</b>	<b>35.36 ± 0.51</b>	<b>54.84 ± 1.54</b>	<b>32.52 ± 0.61</b>

Table A4: **Top-1 Not-Same-Batch (NSB) / Not-Same-Source (NSS) 1-NN retrieval accuracy across the 4 benchmarking settings for the TGT2 test datasets after batch correction post-processing**, identical to the results shown in Figure 6 and reproduced in numerical form for reproducibility purposes. Error bars represent the standard deviation across  $n=3$  replicates with random seeds. Asterisk indicates that MICON significantly outperforms the baseline, defined as  $p < 0.05$  on an unpaired one-tailed t-test with performance across the  $n=3$  random seeds as trials.

TGT-2 (ID)	1-NN NSB (ID)	1-NN NSS (ID)	1-NN NSB (UNSEEN COMPOUND)	1-NN NSS (UNSEEN COMPOUND)
RANDOM CHANCE CELLPROFILER	$11.5 \pm 0.32^*$	$3.16 \pm 0.21^*$	$5.54 \pm 0.23^*$	$3.11 \pm 0.12^*$
SIMCLR CLIP	$9.61 \pm 0.53^*$ $11.69 \pm 0.37^*$	$3.58 \pm 0.15^*$ $3.99 \pm 0.11^*$	$5.32 \pm 0.27^*$ $5.79 \pm 0.26^*$	$2.13 \pm 0.23^*$ $2.36 \pm 0.15^*$
MICON	<b><math>13.85 \pm 0.49</math></b>	<b><math>5.17 \pm 0.18</math></b>	<b><math>7.23 \pm 0.33</math></b>	<b><math>3.98 \pm 0.15</math></b>

Detailed metadata statistics for our POS-CTL and Target-2 dataset splits are available in Tables A5 and A6, including the numbers of unique source, batch, plate, and wells in each split.

Table A5: Detailed metadata statistics for the POS-CTL data splits shown in Figure 3.

	PERTURBATIONS	# SOURCES	SOURCE IDS	BATCHES	PLATES	WELLS	FOVs
ID TRAINING DATASET	8	6	2,3,5,7,8,11	57	679	21284	395279
ID VALIDATION DATASET	8	6	2,3,5,7,8,11	6	139	4305	89988
ID TEST DATASET	8	6	2,3,5,7,8,11	12	283	9078	192094
UNSEEN SOURCES OOD TRAINING DATASET	8	5	3,5,7,8,11	57	756	23752	479556
UNSEEN SOURCES OOD VALIDATION DATASET	8	5	3,5,7,8,11	5	137	4254	92535
UNSEEN SOURCES OOD QUERY DATASET	8	1	2	8	133	4096	60853
UNSEEN SOURCES OOD RETRIEVAL DATASET	8	1	2	5	86	2565	44417

Table A6: Detailed metadata statistics for the Target-2 data splits as shown in Figure 4.

	PERTURBATIONS	# SOURCES	SOURCE IDS	BATCHES	PLATES	WELLS	FOVs
ID TRAINING DATASET	301	10	2,3,4,5,6,7,8,9,11,13	71	92	35156	325834
ID VALIDATION DATASET	301	10	2,3,4,5,6,7,8,9,11,13	10	15	5723	53341
ID TEST DATASET	301	10	2,3,4,5,6,7,8,9,11,13	20	28	10875	99781
UNSEEN COMPOUNDS OOD TRAINING DATASET	301	10	2,3,4,5,6,7,8,9,11,13	91	122	46667	432500
UNSEEN COMPOUNDS OOD VALIDATION DATASET	301	10	2,3,4,5,6,7,8,9,11,13	10	13	5087	46456
UNSEEN COMPOUNDS OOD QUERY DATASET	184	8	2,3,5,6,7,8,9,11	70	324	493	4053
UNSEEN COMPOUNDS OOD RETRIEVAL DATASET	184	8	2,3,5,6,7,8,9,11	54	222	368	3079

Table A7: **Hyperparameters of the MICON architecture.**

Model		Training	
ECP4 fingerprint dimension	2048	optimizer	Adam
image encoder embedding size	1000	batch size	64
image projector hidden size	512	learning rate	1e-3
molecule hidden size	512	warmup steps	2000
fusion module hidden size	512	weight decay	1e-2
final projected embedding size	256	gradient clipping	1.0

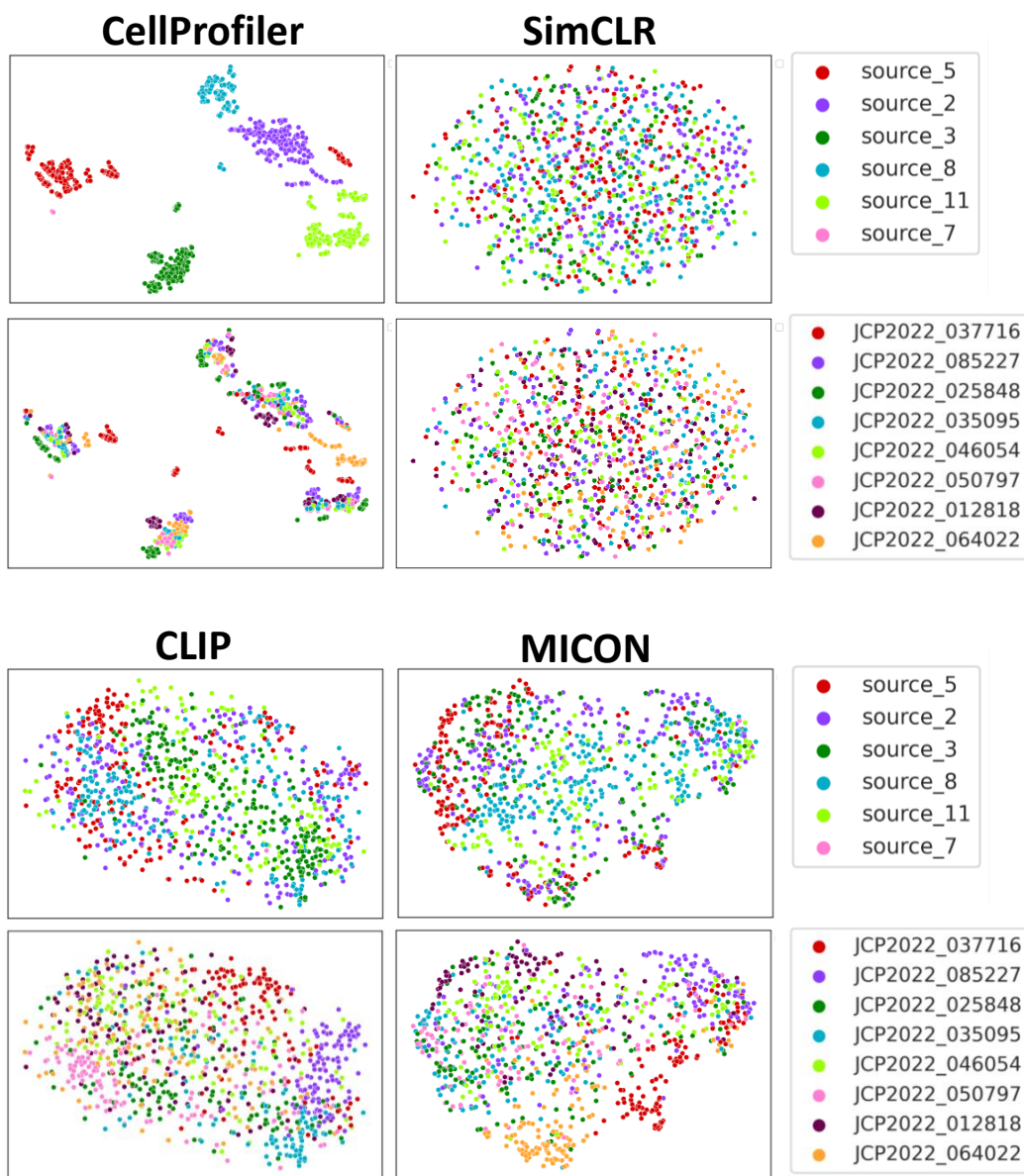


Figure A1: **Image representations from CellProfiler, SimCLR, CLIP, and MICON for the POS-CTL dataset, reduced using UMAP and visualized as a 2D scatterplot.** For each representation method, the top plot is colored by source, and the bottom plot is colored by perturbation, to visualize robustness to batch effects and clustering of biological phenotype, respectively.  $n=2,000$  randomly sampled images are shown.

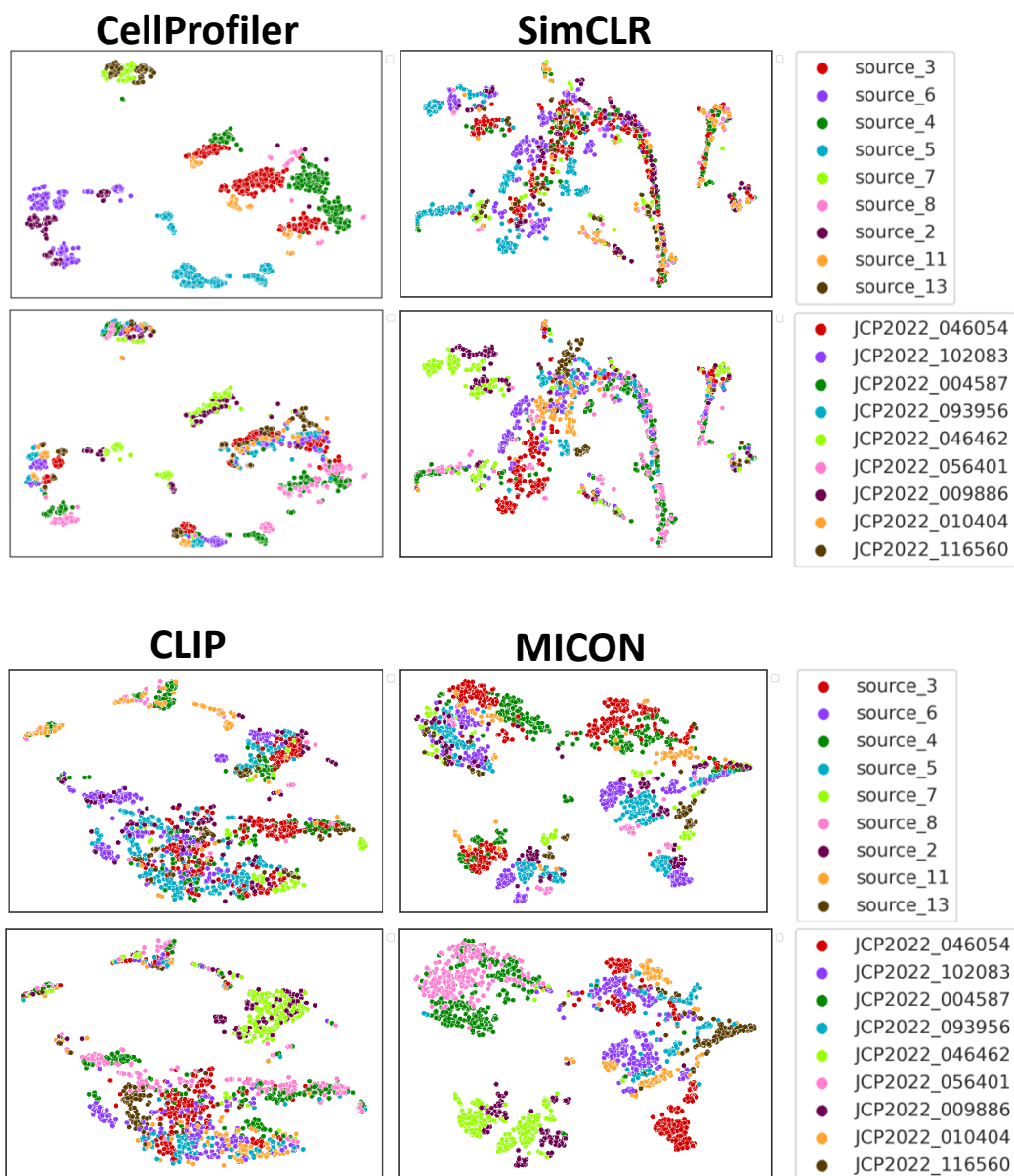


Figure A2: **Image representations from CellProfiler, SimCLR, CLIP, and MICON for a subset of the Target-2 dataset, reduced using UMAP and visualized as a 2D scatterplot.** For each representation method, the top plot is colored by source, and the bottom plot is colored by perturbation, to visualize robustness to batch effects and clustering of biological phenotype, respectively. 10 compounds with accuracy higher than 0% across all methods are randomly sampled to avoid cluttering the visualization with too many labels.  $n=2,000$  randomly sampled images are shown.

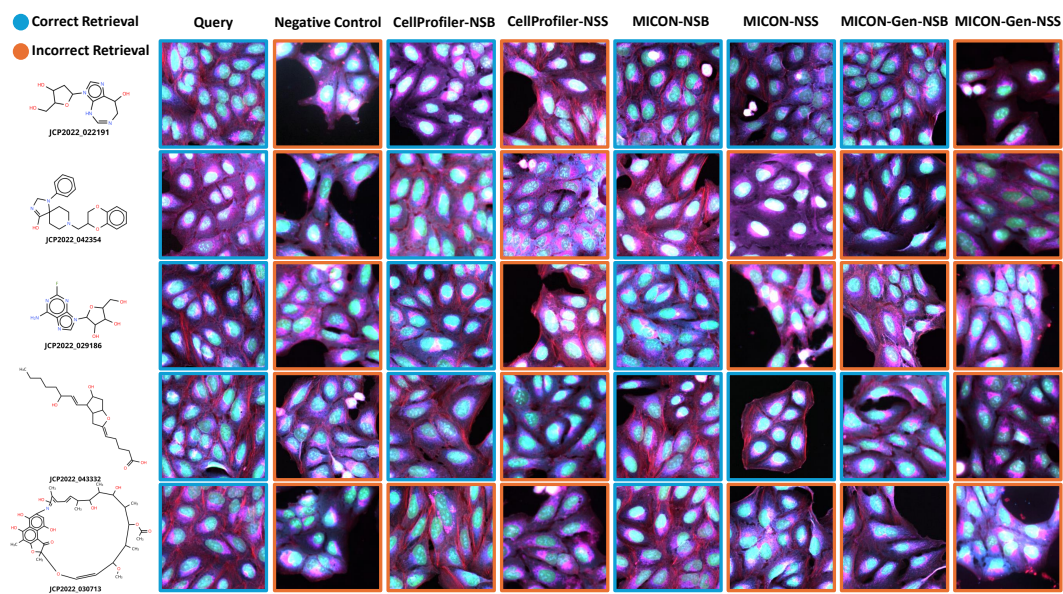


Figure A3: NSB/NSS retrieval results using images sampled from the Target-2 dataset. Representations of the query image (first column) are used to retrieve other images in the dataset. Negative control shows a negative control from the same batch. CellProfiler-NSB and CellProfiler-NSS designate the nearest neighbor of the query image in CellProfiler features in a different batch and source respectively. MICON-NSB and MICON-NSS are these retrievals but using MICON features, while MICON-Gen-NSB and MICON-Gen-NSS are retrievals using generated counterfactual representations. Blue frame images are treated with the same perturbation and orange frames indicate the treatments are from different perturbations/negative control. Channels are colored so that DNA is shown in blue, ER is shown in green, AGP (Actin, Golgi, Plasma Membrane) in red, mitochondria in magenta, and RNA in cyan. Channels are rescaled to the full intensity range of the image. A representative crop is taken for each image.